

## Article

# Deformation and Failure Laws of Surrounding Rocks of Coal Roadways under High Dynamic Load and Intelligent Prediction

Aoran Li, Guangzhen Cui, Peng Wang \*, Xinjie Wang, Zhengtao Hong, Jiangrong Kong and Jiaguang Kan \*

Key Laboratory of Deep Coal Resource Mining of the Ministry of Education, School of Mines, China University of Mining and Technology, Xuzhou 221116, China

\* Correspondence: wangpeng19@cumt.edu.cn (P.W.); jgkan@cumt.edu.cn (J.K.)

**Abstract:** Under high dynamic load, roadway deformation and failure may occur, posing great challenges. As for now, few studies have been carried out on the impacts of various factors on the deformation of roadway surrounding rocks under high dynamic load, not to mention those on intelligent prediction of the deformation and failure laws. This paper fills these research gaps by studying the deformation and failure characteristics of roadway surrounding rocks and the intelligent prediction method under high dynamic load. The finite difference software Flac3D was used to analyze the influences of roadway buried depth, lithology, and side pressure coefficient on the stability of surrounding rocks and a model was constructed for deformation prediction under high dynamic load. Finally, the influence of various factors on the deformation and their weight was obtained and the deformation can be predicted in line with the BP neural network prediction theory. The results show that the prediction effect is good, with high accuracy.

**Keywords:** finite difference analysis; high dynamic load; deformation mechanism of surrounding rocks; deformation influencing factors; prediction of roadway deformation



**Citation:** Li, A.; Cui, G.; Wang, P.; Wang, X.; Hong, Z.; Kong, J.; Kan, J. Deformation and Failure Laws of Surrounding Rocks of Coal Roadways under High Dynamic Load and Intelligent Prediction. *Sustainability* **2023**, *15*, 1313. <https://doi.org/10.3390/su15021313>

Academic Editors: Zhijie Wen, Guolei Liu, Mingshi Gao and Jinhao Wen

Received: 1 December 2022

Revised: 5 January 2023

Accepted: 6 January 2023

Published: 10 January 2023



**Copyright:** © 2023 by the authors. Licensee MDPI, Basel, Switzerland. This article is an open access article distributed under the terms and conditions of the Creative Commons Attribution (CC BY) license (<https://creativecommons.org/licenses/by/4.0/>).

## 1. Introduction

As the coal mining depth continues to deepen, the deformation and damage of deep roadways of coal mines, resulting from the superposition of mining stress caused by coal mining, has become an increasingly serious challenge. Consequently, the massive deformation of roadways due to high dynamic load, and even the number of related accidents, has been on the rise dramatically. Therefore, it will be of great significance to explore the deformation and failure mechanisms of roadways under high dynamic load for better performance of surrounding rocks of deep roadways.

The high dynamic load in coal mines is mainly derived from the mine earthquake phenomenon produced in the mining process [1] and can lead to the sudden instability and destruction of surrounding rock, causing rock bursts on the working face and threatening the safety of mine production. At present, the research on the deformation and failure mechanisms of roadway surrounding rocks under high dynamic load mainly consists of field investigation, theoretical analysis, numerical simulation, and physical model testing [2–11], among which the numerical simulation method has been widely used. At present, Flac3D/Udec and other software are considered effective tools for simulating the dynamic phenomena of mines under the action of dynamic load [12–15], which can not only analyze the influences of various factors on the deformation and failure processes of roadway surrounding rocks under high dynamic load in actual constructions [16–19] but can also simulate the deformation and failure of complex roadways under high dynamic load [20–23]. Xiao [24] established a mechanical model to explore roadway floor impact-related instability of deep roadways, based on which the energy criteria for judging roadway floor impact-related instability were acquired. As Xiao argued, the horizontal stress of roadway floors plays a major factor in inducing floor impact. By constructing a mechanical model of circular roadways,

Feng [25] discussed the influence of confining pressure ratio on the range of plastic zones in roadways, focusing on the impacts of mining on the deformation and failure of mining roadways. Wang [26] established a model for major roof structures typical of fracture lines at different positions above the coal rib, based on which the structural conditions for dynamic load impacts on major roofs and the expression of impact force were obtained. In combination with an actual engineering case, Wang [27] expounded on the failure mode of surrounding rock instability of composite roofs of coal roadways under the influences of multiple dynamic load disturbances, leading to the conclusion that high dynamic load will significantly aggravate the damages of composite roof roadways in degree. By simulating the impact process of coal and rock roadways induced by disturbance waves, Chen [28] figured out the relationship between the deformation of roadway surrounding rocks and the loading level and strength of flexible waves, revealing that the damages associated with the risk of high dynamic load in the outer side of the roadway are minor compared with those in the inner side. Zhang [29] pointed out that, under the conditions of hard roofs and floors, the hardness and thickness of coal seams are highly influential on the occurrence of high dynamic load. According to Zhang [30], the lithology of overlying strata and coal seams exerts significant impacts on the formation of crack structures in roadway surrounding rocks, and the surrounding rocks under the condition of high-strength stress waves are more likely to have spallation structures that would easily induce high dynamic load damages. The existing studies mainly focus on the exploration of the deformation and failure laws of roadway surrounding rocks under high mining or impact dynamic pressure, as well as the influence of impact energy on the stability of surrounding rocks [31,32]. By contrast, few studies are dedicated to the impacts of various factors on the deformation of roadway surrounding rocks under high dynamic load. For instance, He [33] obtained the dynamic process of roadway deformation and failure under strong mining and low surrounding rock strength conditions. Zhao [34] studied the damage of different impact loads on the internal and microstructure of coal rock. At present, reports on the intelligent prediction of the deformation and failure laws are also rare. If the deformation and damage of the roadway surrounding rock under the action of strong dynamic load can be accurately predicted, the roadway disaster prevention can be accurately controlled, thus effectively improving the safety performance of the roadway.

Based on the actual engineering geological conditions of a typical kilometer-deep mine featured with high dynamic load in China, the dynamic module of Flac3D numerical simulation software was used in this experiment to simulate and analyze the stress distribution, deformation characteristics, plastic zone distribution, and influence law of roadway surrounding rocks under dynamic load. The influences of roadway buried depth, coal seam, roof strength, and surrounding rock side pressure coefficient on the deformation of roadway surrounding rocks under high dynamic load were studied and analyzed in an innovative manner. A model was constructed to predict the deformation of roadway surrounding rocks under high dynamic load based on the BP neural network prediction theory, which revealed favorable accuracy and reliability of the method.

## 2. Scheme of Numerical Simulation Research

The finite difference software Flac3D, which is used to simulate a series of changes in roadway surrounding rocks under the action of high dynamic load, can not only analyze the elastoplastic and large deformation of the materials effectively but can also perform three-dimensional and complete dynamic analysis through the dynamic module. Therefore, it is considered a tool more suitable for simulating demands in this regard. This experiment mainly aims to simulate the processes for the changes in stress and deformation of roadway surrounding rocks under high dynamic load, in addition to its exploration of the stress distribution and deformation law of roadway surrounding rocks after the impact of high dynamic load.

### 2.1. Rock Stratum Parameters

This paper mainly takes the 7303 working face as the simulation background, the working face plan is shown in Figure 1. The prototype roadway is a straight wall micro-arch; the net width of the section is about 6 m; the net height is about 4 m. The main coal seam of the working face is the 3 coal, with a thickness of 1.4~8.7 m and an average thickness of 6.7 m. Under strong dynamic load, the coal rock mass has low strength, and large area crushing can easily occur. The coal seam roof is mainly mudstone and the basic top is siltstone, fine sandstone, and a middle sandstone interlayer. The main lithology is mudstone, siltstone, and a certain mudstone siltstone interlayer and the basic bottom is mainly silty sandstone. The geological conditions are shown in Table 1.

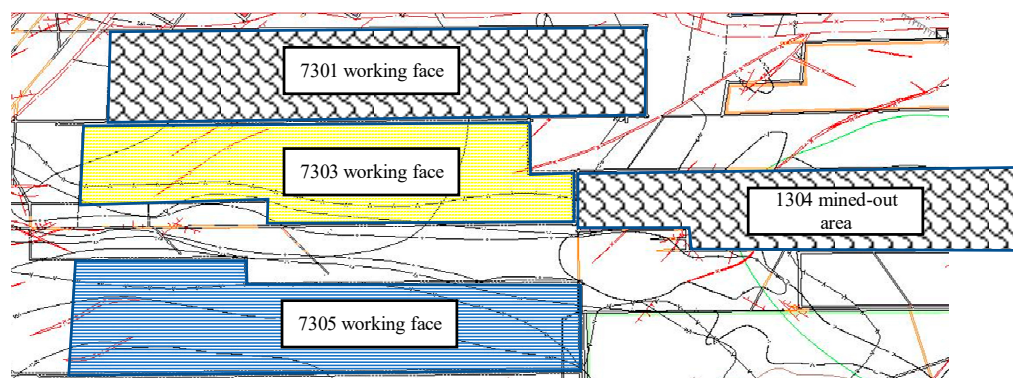


Figure 1. 7303 working face plan.

Table 1. Geological conditions.

| Rock Stratum Information | Lithology                           | Depth of Stratum | Lithological Characteristics   |
|--------------------------|-------------------------------------|------------------|--|
| Main roof                | Medium sandstone and fine sandstone | 4.5~12.92        | Gray–white medium sandstone with argillaceous inclusion<br>Light grayish green fine sandstone with locally broken core |
| Immediate roof           | Mudstone                            | 0.4~3.86         | Black mudstone that is relatively broken<br>Dark grey mudstone with blocky and shelly fractures                        |
| Direct bottom            | Mudstone and silty fine sandstone   | 0.0~11.76        | Black siltstone with horizontal bedding<br>Gray siltstone that is partially broken                                     |
| Basic bottom             | Silty fine sandstone                | 10.3~11.9        |  |

### 2.2. Model Parameters

The experimental numerical model was established using Flac3D, a kind of finite difference software, based on related geological data. Figure 2 presents the length, width, and height of the model, which stood at 66 m, 10 m, and 60 m, respectively. The coordinate origin was located at the lower left corner of the model. The X-axis was perpendicular, while the Y-axis was parallel to the extension direction of the roadway, with the gravity direction of the roadway treated as the Z-axis. The experimental roadway, situated in the coal seam and having a rectangular section, was 6 m in width and 4 m in height. The model had a total of 39,600 nodes. At the top of the model, an identical load was applied to the overlying strata, which were as thick as 400 m with an averaged bulk density of 25 KN/m. See Figure 3, horizontal displacement constraint and fixed constraint were applied to the side and the bottom of the model, respectively. Table 2 presents the mechanical parameters of the rock adopted in the experiment.

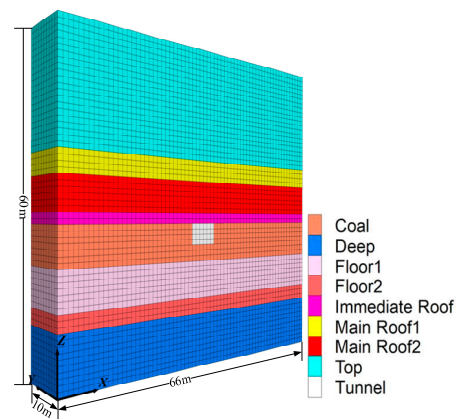


Figure 2. Three-dimensional model of the roadway.

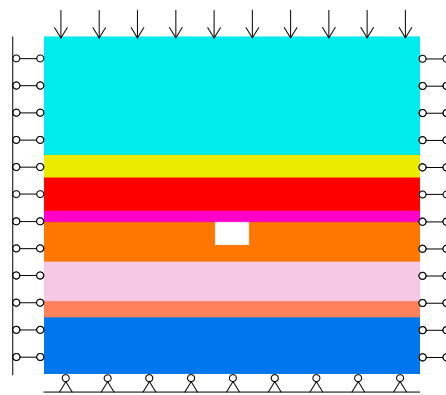


Figure 3. Boundary conditions of the model.

Table 2. Parameters of rock mass model.

| Name             | Lithologic Characteristics | Bulk Modulus/GPa | Shear Modulus/GPa | Poisson's Ratio $\nu$ | Internal Friction Angle $\varphi/^\circ$ | Cohesion $c/\text{MPa}$ |
|------------------|----------------------------|------------------|-------------------|-----------------------|--|-------------------------|
| Overlying strata | Mudstone                   | 9.01             | 4.64              | 0.28                  | 35                                       | 3.12                    |
| Main roof        | Medium sandstone           | 12.22            | 7.33              | 0.25                  | 30                                       | 3.86                    |
|                  | Fine sandstone             | 10.52            | 6.31              | 0.25                  | 30                                       | 4.12                    |
| Immediate roof   | Mudstone                   | 9.01             | 4.64              | 0.28                  | 35                                       | 3.12                    |
| Coal seam        | Coal                       | 4.75             | 1.82              | 0.33                  | 28                                       | 2.43                    |
| Direct bottom    | Mudstone                   | 9.01             | 4.64              | 0.28                  | 35                                       | 3.12                    |
| Basic bottom     | Siltstone                  | 8.98             | 5.78              | 0.2                   | 38                                       | 3.75                    |

### 2.3. Dynamic Loading Scheme

A rock burst event occurred in the mine when the dynamic load energy reached about  $10^5$  J, at which the dynamic load shear wave generated a normal stress of approximately 20 MPa [35]. Existing studies have shown that when the impact stress propagates to a certain distance, it can be simplified as a stress harmonic wave [36]. Based on this theory, it was proposed herein to simplify the  $10^5$  J dynamic load energy into a simple harmonic wave and load it on the top of the model. Figure 4 shows the simplified harmonic, the peak of the simplified harmonic wave was recorded as 25 MPa, with a fluctuation range of 15 MPa~25 MPa and a disturbance period of 0.02 s. With Rayleigh damping set as the mechanical damping of the model, the boundaries at the bottom and around the roadway were designed as the static boundary to absorb the reflected waves before the loading of the power. A monitoring point was arranged every 0.5 m around the roadway for observation of stress distribution and deformation around the roadway. After the static balance, the balance of the roadway excavation was solved and then the dynamic calculation was conducted. Specific settings are shown in Figure 5.

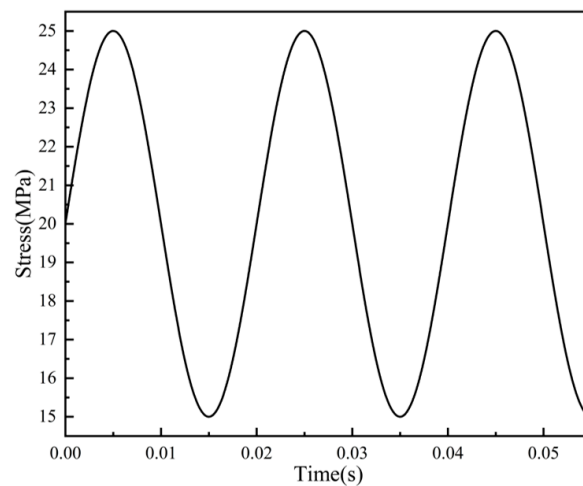


Figure 4. Time history curve.

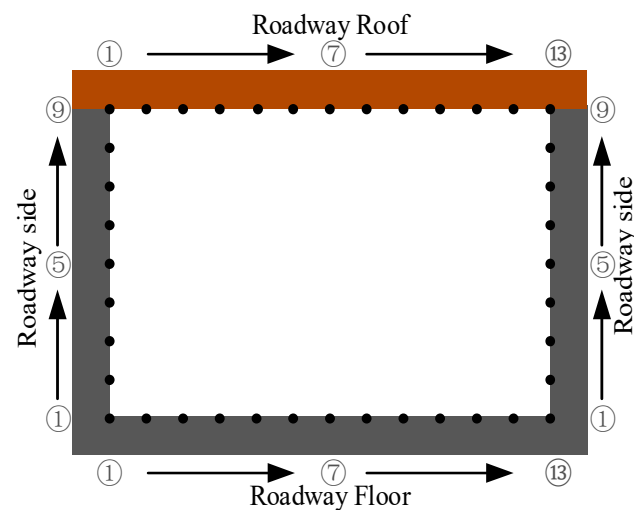
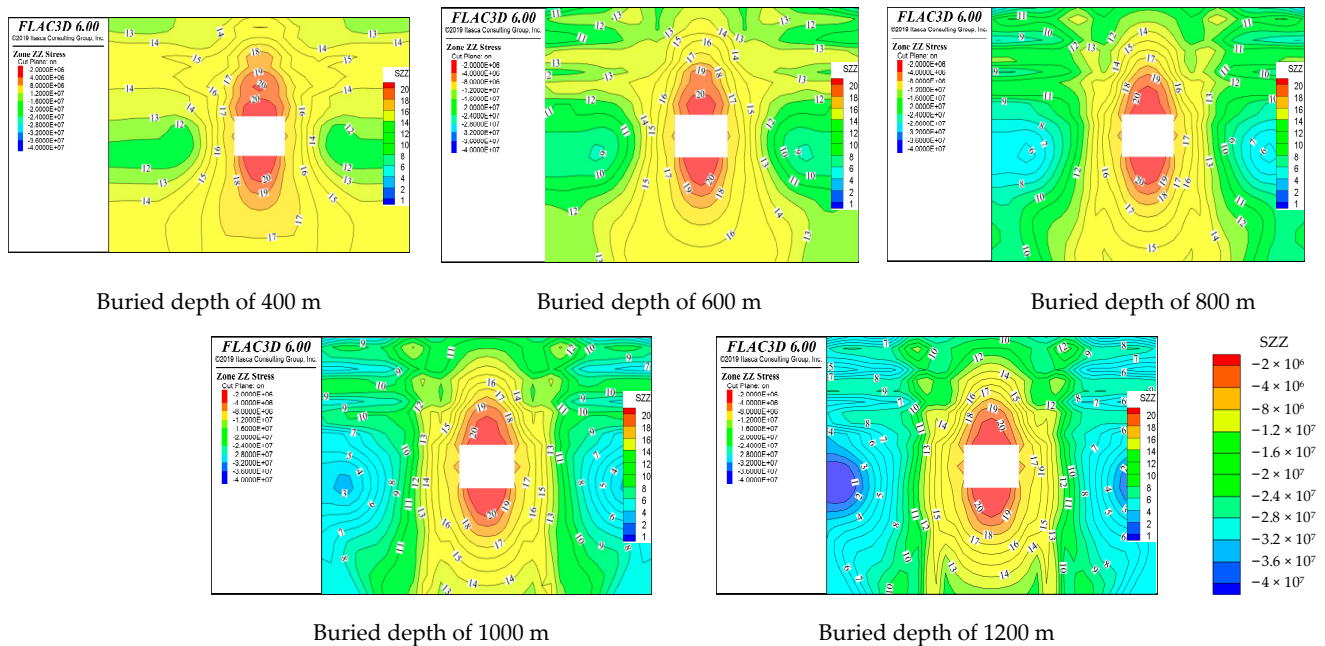


Figure 5. Monitoring point diagram.

### 3. Discussion and Analysis of Results

#### 3.1. Influence of Buried Depth on Deformation and Failure of Surrounding Rocks

Figure 6 presents the stress cloud diagram of roadway surrounding rocks at different buried depths. The range of the stress concentration area at both sides gradually expanded as the buried depth of the roadway deepened. The maximum vertical stress in the stress concentration area increased by about three levels, namely 6 MPa, for every increase of 200 m in buried depth. However, the position of the vertical stress extreme value outside the two sides of the roadway was detected further away from the roadway as the buried depth of the roadway deepened. Given a buried depth of 400 m, the position of the vertical stress extreme value was 7 m away from the two sides of the roadway. When the buried depth reached 1200 m, however, the position of the vertical stress extreme value was about 14 m away from the two sides of the roadway. The stress gradient around the roadway increased dramatically as the buried depth deepened, alongside a more intensive stress distribution contour around the roadway.



**Figure 6.** Vertical stress nephogram of the roadway at different buried depths.

The range of the stress reduction area in yellow around the roadway shrank to a final shape of H in a gradual process as the buried depth deepened. Extremely small stress was observed at a buried depth between 5 and 8 m, where the two bottom angles of the roadway extended downward. The stress was measured as 16 at a buried depth of 400 m. At a buried depth of 1200 m, the stress stood at 14 and only increased by a relatively small amount of about 4 MPa.

See Figure 7, as the buried depth of the roadway deepened, the maximum deformation of the roof of the roadway unexceptionally increased at a rate between 111 and 113%, with the maximum variation rate of the side reaching 160%. Though the maximum deformation differed significantly between the roof and the side, the differences in the maximum deformation of the floor before and after the experiment were within a range of 0.15 m, indicating that the buried depth had a minor impact on the deformation of the floor. Nevertheless, the maximum deformation of the roof and the side of the roadway was more susceptible to changes in buried depth. As shown in Figure 7c, the deformation at the top corner of the roadway was prominently smaller than that at the bottom corner under the condition of a large buried depth. Given a buried depth of 1200 m, the maximum deformation of the roof and the side exceeded 1.5 m and 1.7 m, respectively.

As shown in Figure 8, the increase in the buried depth of the roadway led to the gradual expansion of the plastic zone around the roadway into a shape of “butterfly” as a whole, accompanied by the gradual propagation of the shear failure zone outward along the top and bottom angles of the roadway. At a buried depth of 400 m, a tensile failure area appeared at a depth of 3~12 m underneath the bottom angle of the roadway. Meanwhile, the maximum extension range of the plastic zone reached 7 m in the upper limit and 12 m in the lower limit, and the coal seam area witnessed a shear failure to a certain degree. As the buried depth continued to deepen, the tensile failure area underneath the bottom corner of the roadway gave way to a shear failure area in a gradual process, in spite of the existence of a small tensile failure area within 1 m around the roadway. When the buried depth reached 1200 m, the maximum extension range of the plastic zone reached 12 m in the upper limit and 19 m in the lower limit. As the buried depth grew deeper, the plastic zone around the roadway eventually expanded outward.

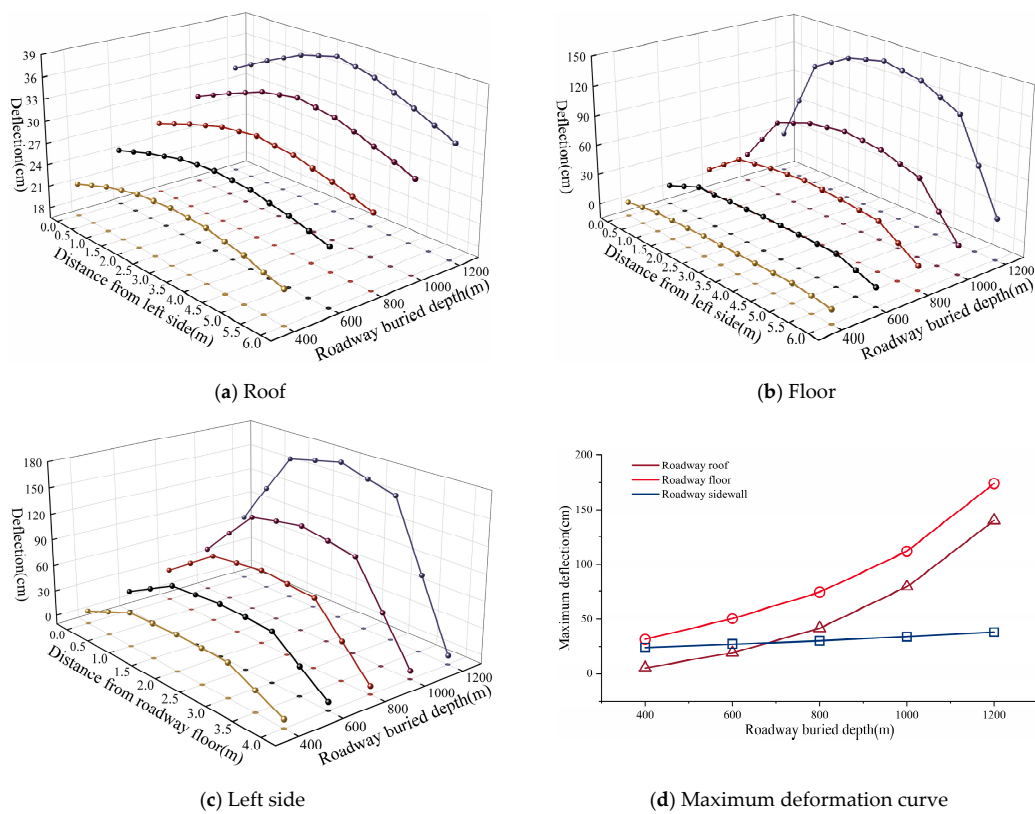


Figure 7. Roadway deformation at different burial depth.

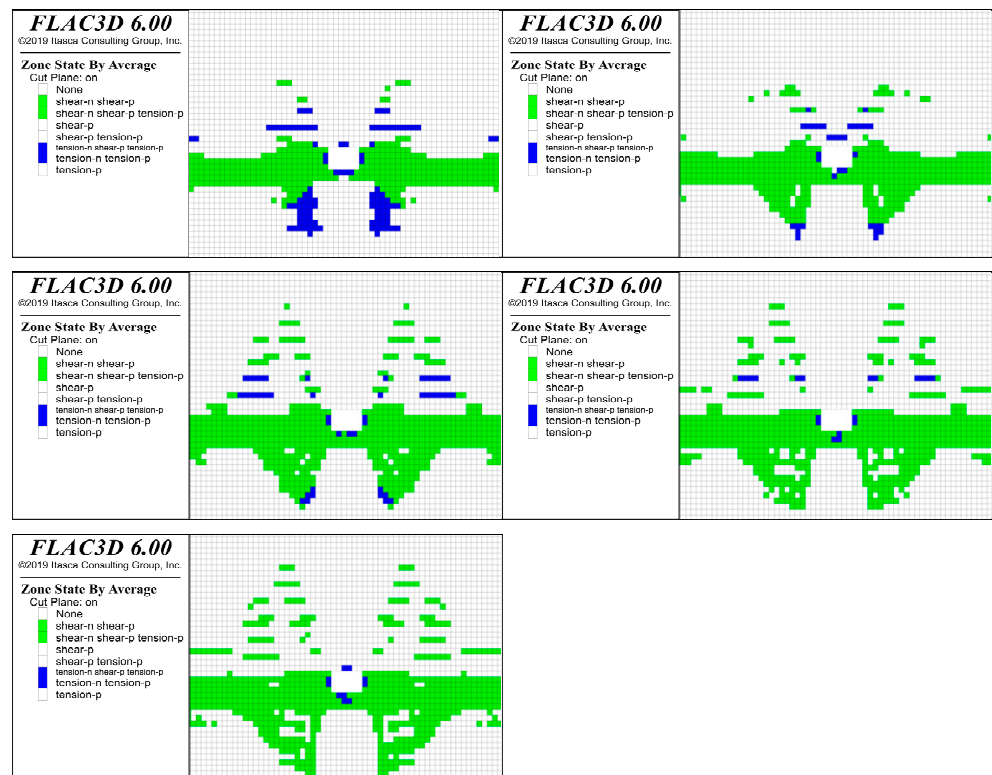


Figure 8. Distribution of roadway plastic zones at different tunnel burial depths.

### 3.2. Influence of Surrounding Rock Strength on Deformation and Failure of Surrounding Rocks

The roadway simulated in this experiment is a coal–rock roadway with a roof composed of mudstone with relatively high strength. The coal seam and the roof rock layer were divided into six grades based on strength to explore the changes in lithology of the surrounding rock of the roadway, the parameters are shown in Table 3. It was revealed that the peak vertical stress of roadway surrounding rocks at different coal seam strength grades differed significantly, in contrast with smaller differences under the conditions of different roof rock strength grades. As shown in Figure 9a,  $C6 > C5 > C4$  (original parameter)  $> C3 > C2 > C1$  in terms of the rank of peak vertical stress load [37] and the stress concentration point moved towards the roadway as the coal strength increased in a gradual process. Under the condition of C1, the peak stress at the center of roof was 3.34% of the original rock stress and the overall roof vertical stress ranged between 3.34 and 50.46% of the original rock stress. Under the condition of C6, the peak stress at the center of roof was 1.91% of the original rock stress, with the overall roof vertical stress ranging between 1.91 and 87.93% of the original rock stress; it can be explained that the increase of coal seam strength contributed to the stability of roadway roof under high dynamic load. Apparently, as the coal seam strength rose, the vertical stress gradually decreased at the center of the roof, while increasing on the two sides. As the roof rock strength grew, the stress concentration factor increased in value in a gradual process, while the amplitude remained comparatively small, in spite of insignificant changes in stress concentration position.

**Table 3.** Rock stratum parameter simulation scheme.

| Mechanical Parameters | Roof Stratum |      |      |      |      |      | Coal Seam |      |      |      |      |      |
|-----------------------|--------------|------|------|------|------|------|-----------|------|------|------|------|------|
| Grade                 | I1           | I2   | I3   | I4   | I5   | I6   | C1        | C2   | C3   | C4   | C5   | C6   |
| Elastic modulus/GPa   | 4.8          | 5.9  | 7.9  | 9.9  | 11.9 | 13.9 | 1.8       | 2.8  | 3.8  | 4.8  | 5.8  | 6.8  |
| Poisson's ratio       | 0.31         | 0.31 | 0.30 | 0.29 | 0.28 | 0.27 | 0.36      | 0.35 | 0.34 | 0.33 | 0.32 | 0.31 |
| Cohesion/MPa          | 1.02         | 1.32 | 1.92 | 2.52 | 3.12 | 3.72 | 1.83      | 2.03 | 2.23 | 2.43 | 2.63 | 2.83 |

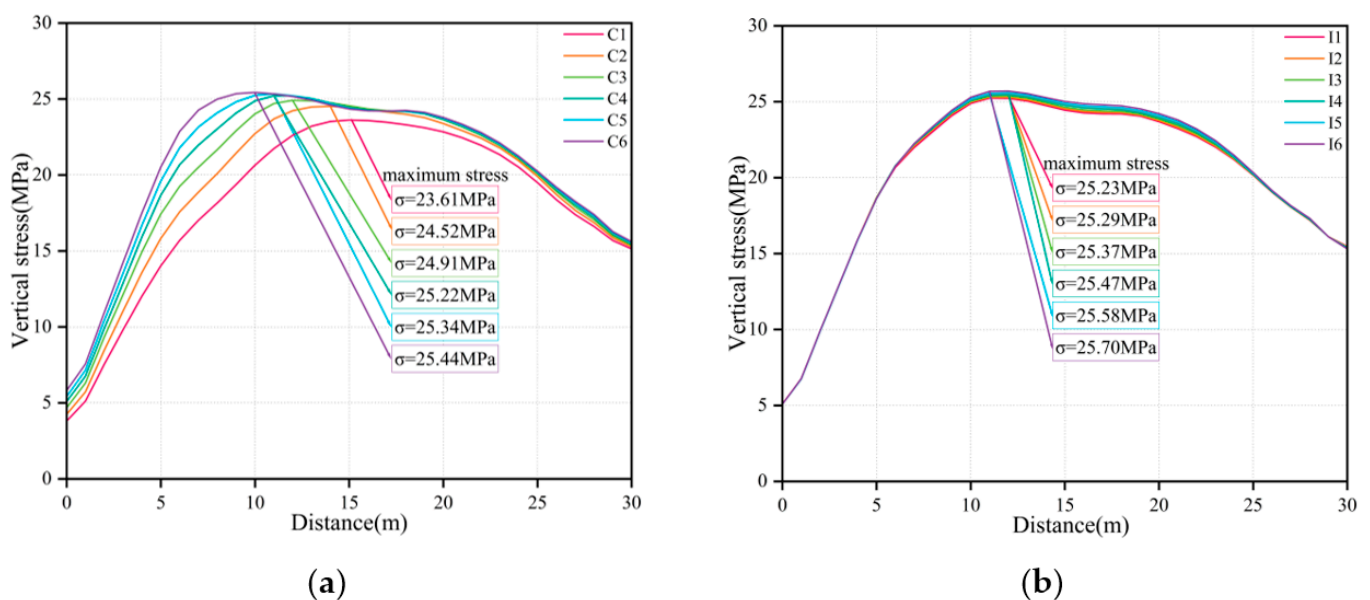


**Figure 9.** (a) Stress concentration degree of different coal seam grades. (b) Stress concentration degree of different rock stratum grades.

As shown in Figures 10 and 11, the increase in roof strength or coal seam strength limited roadway roof deformation effectively. When the elastic modulus of the roof stratum varied from 5.9 MPa to 4.8 MPa (i.e., equal to the elastic modulus of the coal seam), though variations in roof strength decreased in range, sharp deformation took place at the center of the roof, which was much larger than the deformation at the center of the roof when the

roof elastic modulus reached 5.9 MPa. In the meanwhile, a decreasing trend was observed in the deformation at both ends of the roadway roof.

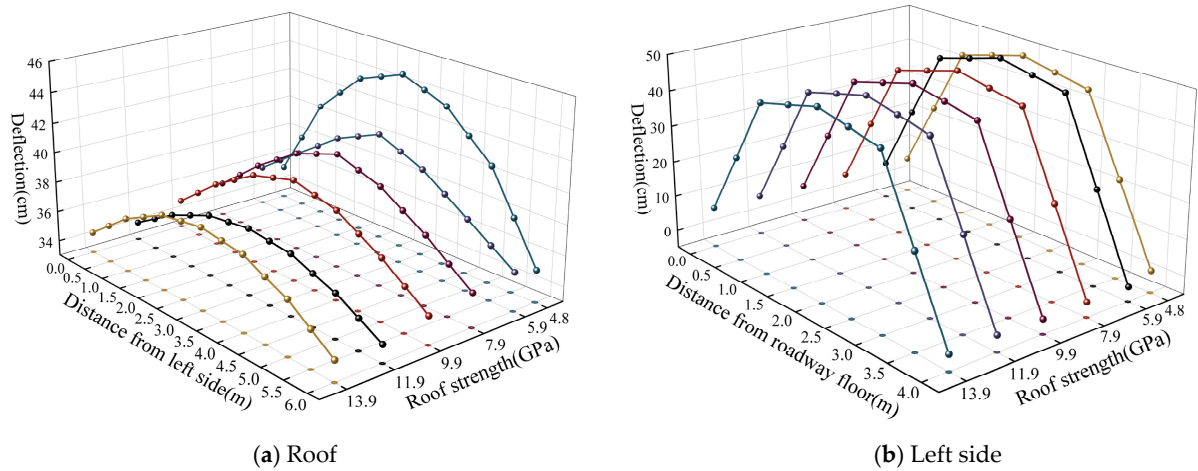


Figure 10. Roadway deformation under different roof strength conditions.

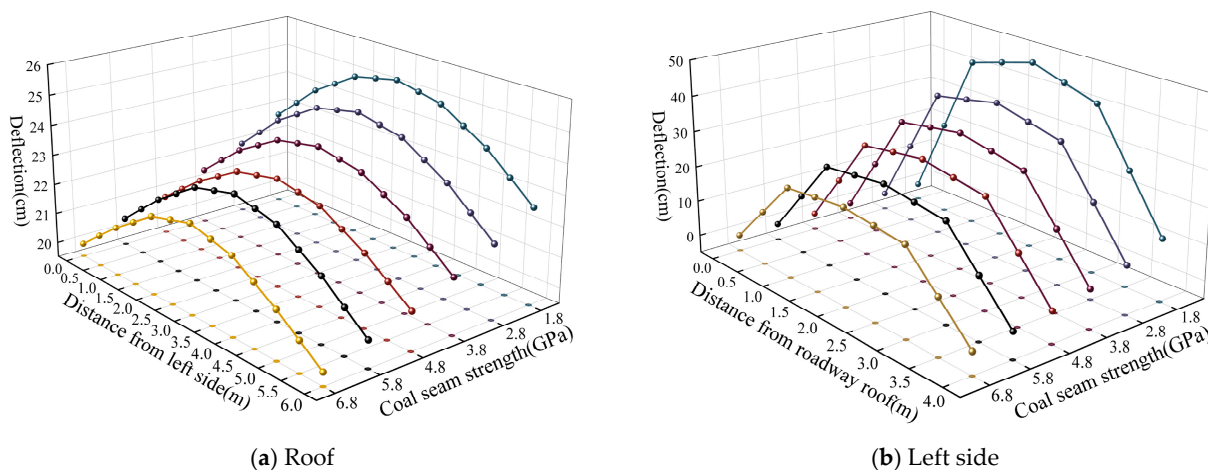


Figure 11. Roadway deformation under different coal seam strength conditions.

Deformation direction of the side wall and roof of the roadway moved toward the interior of the roadway, in addition to an identical pattern in deformation. As shown in the diagram, the deformation along the vertical direction at the intersection of the roadway roof and the side was much greater than that along the horizontal direction. Given a coal seam strength at a certain value, the deformation along the horizontal direction was almost negligible. When the coal seam strength was less than 5.8 MPa, the deformation extreme value of the roadway side always exceeded that of the roadway roof. Furthermore, as the coal seam strength grew, the extreme value gradually dropped to a smaller value than that of the roadway roof.

Similarities were observed in the plastic failure of roadway surrounding rocks under different surrounding rock strength conditions. Shear failure was revealed as the major failure mode, with the shear failure areas mainly concentrated in the coal seam. Tensile failure areas appeared in the area above the roadway as the coal strength rose. When the roof rock strength increased, the shear failure area around the roadway exhibited a tendency to decrease. It was shown that high coal seam strength could effectively reduce the range of the plastic failure area and the increase in roof rock strength could effectively prevent the plastic zone from propagating beyond the roof.

### 3.3. Influence of Side Pressure Coefficient on Deformation and Failure of Surrounding Rocks

It can be seen from Figure 12. that an increase in horizontal stress, namely the increase of side pressure coefficient in value, led to the gradual growth of horizontal and vertical stress concentration areas at both sides of the roadway, all of which were transferred to the direction of the roadway. The horizontal stress concentration area came into being right above the roadway in a gradual process. As shown in the horizontal stress contour map, when the side pressure coefficient reached 1.4, the blue area (i.e., the high-stress area) appeared 15 m above the roadway, through an obvious increase in stress could also be observed in the area directly below the roadway.

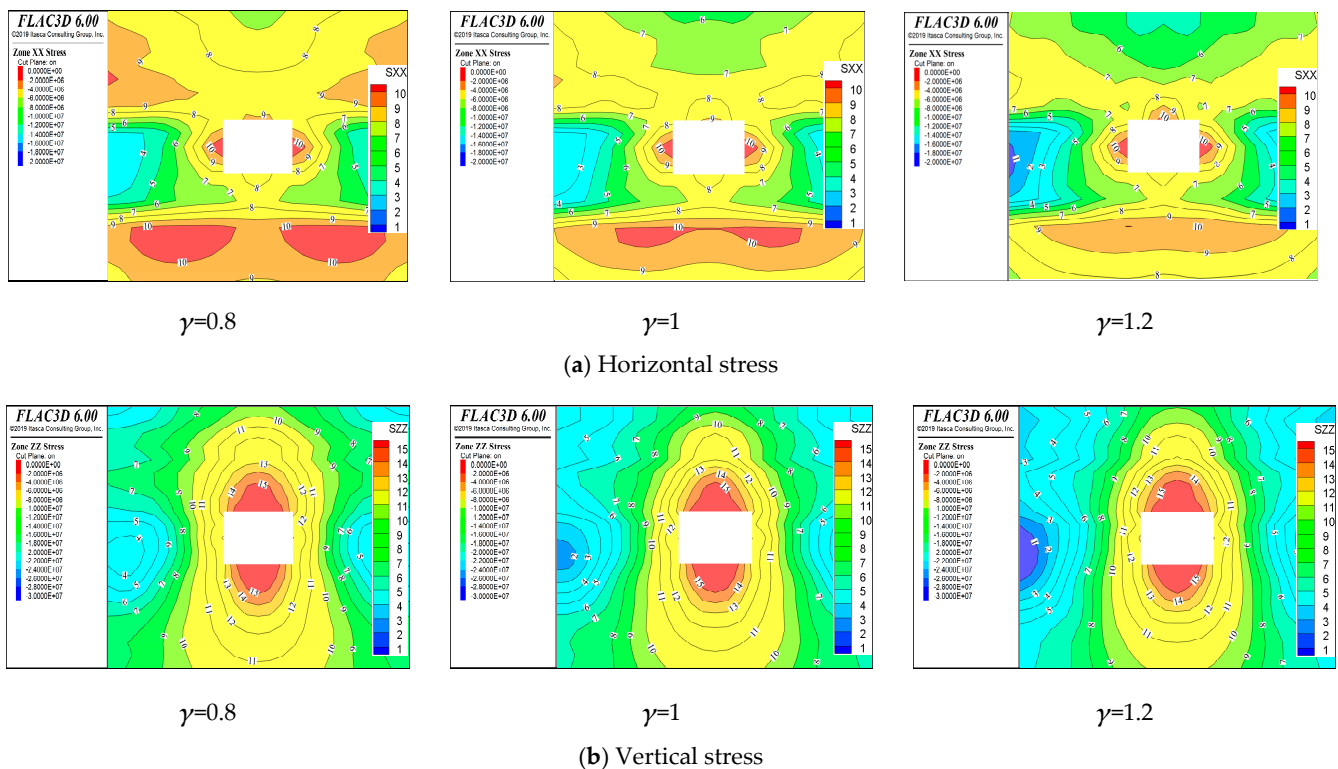


**Figure 12.** Cloud chart of roadway surrounding rock stress under different side pressure coefficient conditions.

When the side pressure coefficient  $\gamma$  stood at 0.8, the peak value of the horizontal and vertical stress in the divided area was measured as 15.3 MPa and 25.2 MPa, respectively, with the peak value detected at a certain distance horizontally from both sides of the roadway. The horizontal stress increased as the distance from the side of the roadway enlarged. When the vertical stress reached the peak at about 8.5 m from the roadway, the vertical stress decreased gradually as the distance from the roadway enlarged. The major stress concentration area remained within the coal seam no matter whether it was associated with the horizontal stress or the vertical stress. As shown in the vertical stress contour map, the pressure relief areas above and below the roadway shrank in range as the side pressure coefficient increased in value and, subsequently, gathered near the roadway in a gradual process. The vertical stress on the two sides of the roadway remained at a much higher level than that above and below the roadway.

The rise in buried depth, side pressure coefficient, and surrounding rock strength increased the degree of stress concentration, among which the rise in buried depth of the roadway influenced the increase in stress concentration intensity substantially. In the meanwhile, the rise in buried depth of the roadway caused the maximum stress concentration point to move towards the direction of the principal roadway, while the rise in coal seam strength caused the maximum stress concentration point to shift towards the

direction of the roadway. Nevertheless, their influences on stress concentration coefficient were relatively small.

Given different side pressure coefficients, large tectonic stress around the roadway but relatively fragile lithology of the coal seam were observed. Therefore, the deformation around the roadway under the action of dynamic load would be massive. Under such circumstances, to guarantee reasonable results, the time for loading was reduced to two cycles during the observation of the deformation law of the roadway as the side pressure coefficient varied. The maximum deformation curves of the roof, floor, and side of the roadway are shown in Figure 13.

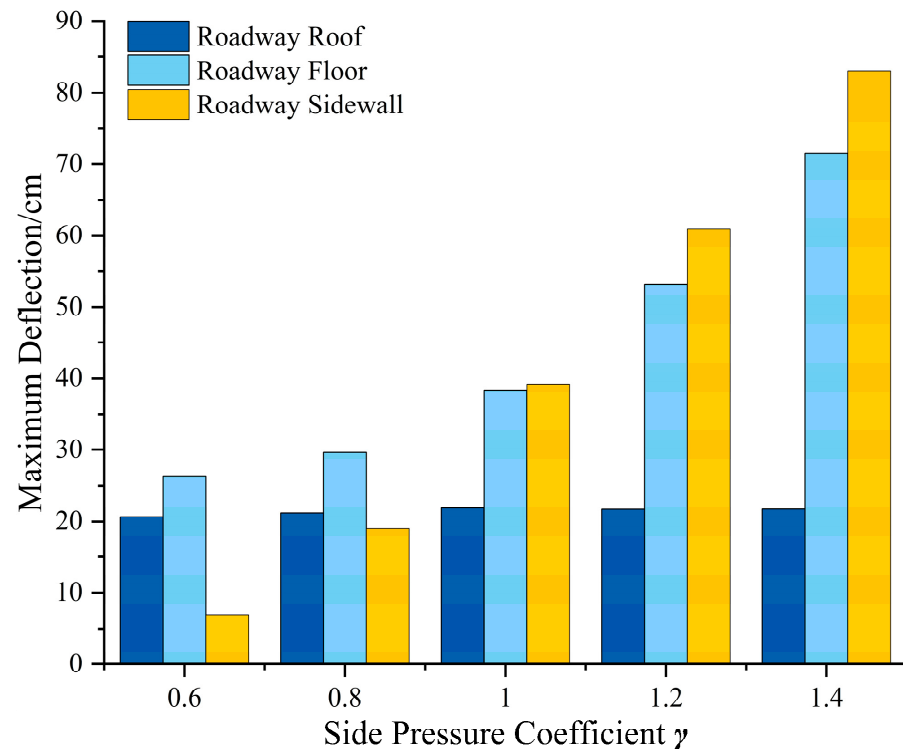


**Figure 13.** Roadway maximum deformation under different side pressure coefficient conditions.

As shown in the figure, when the side pressure coefficient increased in a uniform manner, the maximum deformation of the floor and side wall of the roadway grew as a result, with the rising trend of the maximum deformation of the floor larger than that of the side wall. When the side pressure coefficient  $\gamma$  was below 1, the maximum deformation of the bottom plate was unexceptionally lower than that of the upper plate. When the side pressure coefficient  $\gamma$  stood at 1, the maximum deformation of the bottom plate and the upper plate was almost the same. When the side pressure coefficient  $\gamma$  was greater than 1, the maximum deformation of the bottom plate started to exceed the upper plate. However, nearly no changes in maximum deformation of the roof, which basically remained at about 0.21 m, were detected as the side pressure coefficient varied.

The variations in the side pressure coefficient influenced the deformation of the side dramatically, in contrast with its influence on the deformation of the roof that was almost unaffected. The deformation trend of the roof differed from that of the floor and the side. This may be attributed to the higher strength of the roof stratum and the lower strength of the coal seam, which led to smaller impacts of the changes in the side pressure coefficient on the deformation of the roof. The impacts of different side pressure coefficients on plastic failure were also comparatively small, as evidenced by their only effect in reducing the plastic failure range to a certain extent.

#### 4. Intelligent Prediction of Roadway Deformation Law

The error feedback learning algorithm was adopted to train the model based on the sample data in a BP neural network prediction test, in which the weights and thresholds in the model were modified in a constant manner. The error function decreased along the negative gradient direction, so the model results were considered close to the desired outputs. A neural network prediction model was used to predict the maximum deformation of the roadway roof, with the maximum deformation of the roadway roof under conditions of different buried depths, roof strength, and coal seam strength extracted accordingly. Of all the data obtained, 90% were used as the training sample of the prediction model, while the remaining 10% were used as the prediction sample. The data were applied to the training and prediction of the BP neural network after normalization.

A three-layer BP neural network prediction model was established, with three nodes set in the input layer. The three nodes, namely the buried depth of the roadway, the strength of the roof, and the strength of the coal seam, were considered three factors that affected the deformation of the roadway. The output layer of the model was designed to have one node, namely the maximum deformation of the roof. In the BP neural network prediction model, the number of hidden layers and the number of nodes in each hidden layer affected the accuracy of the prediction results dramatically. In case of a small number of hidden layer nodes, the prediction model might fail in obtaining a learning ability high enough for prediction, leading to decreased prediction accuracy as a result. The absence of too many nodes, however, would make the prediction model more complicated, bringing a higher possibility of local minima of the BP neural network and a slow learning process. The range of hidden layer nodes of the model can be calculated through empirical Formula (1):

$$\text{Hiddennum} = \text{sqrt}(m + n) + a \quad (1)$$

In the formula,  $m$  stands for the number of input layer nodes;  $n$  denotes the number of output layer nodes;  $a$  is a constant, usually an integer from 1 to 10.

After the range of hidden layer nodes was acquired, the number of hidden layer nodes was determined according to the training conditions of the model, after which the number of hidden layer nodes was sorted through comparison of mean square errors. The results are shown in Table 4:

**Table 4.** Selection of hidden layer nodes.

| Number of Nodes | Mean Square Error | Sort | Number of Nodes | Mean Square Error | Sort |
|-----------------|-------------------|------|-----------------|-------------------|------|
| 6               | 0.00074055        | 1    | 5               | 0.0013225         | 6    |
| 4               | 0.0010707         | 2    | 7               | 0.0015081         | 7    |
| 8               | 0.0011019         | 3    | 9               | 0.0027027         | 8    |
| 3               | 0.0011651         | 4    | 11              | 0.0067611         | 9    |
| 10              | 0.0011763         | 5    | 12              | 0.071536          | 10   |

According to Table 4, the model had the best training effect when the number of hidden layer nodes was at six. Therefore, six was determined as the number of hidden layer nodes.

The Trainlm training function [38] was selected as the training algorithm for the model. Since the training function has the advantages of fast convergence speed and high prediction accuracy, it is widely used in geotechnical engineering. The prediction performance of the model was evaluated by comparing such parameters as mean absolute error and mean square error that were parts of the prediction results of the model. The training quantity of the model was set to be 1000, with a learning rate of 0.01 and a minimum prediction error of 0.000001 during the training of the model. Figures 14–16 present the correlation analysis images of the sum of the sample sets of each parameter, the training error decline curve, and the neural network training process, respectively. Apparently, the error of the model reached the expected value after 17 times of iterative training.

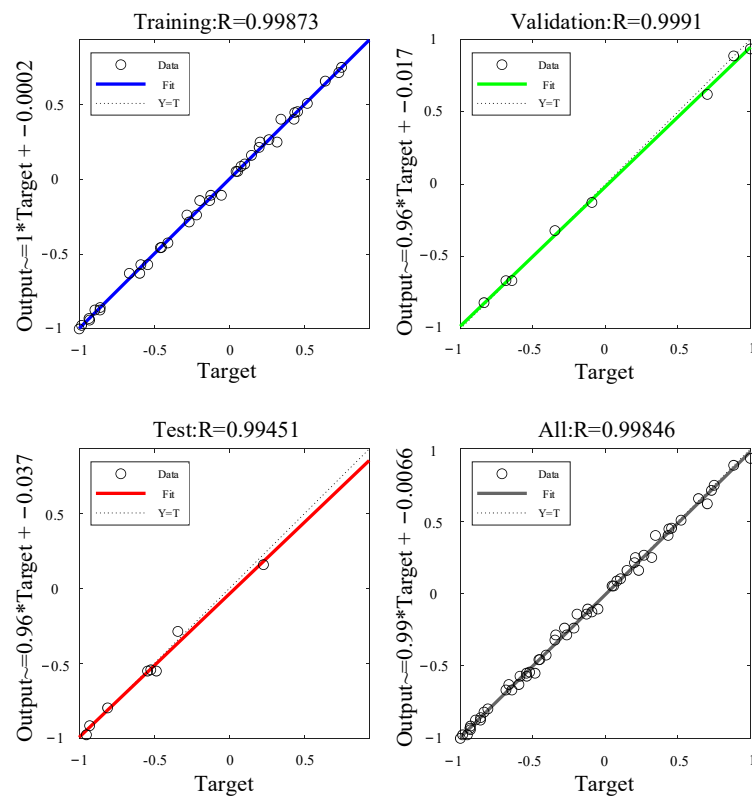


Figure 14. Correlation analysis image of the sum of sample sets of each parameter.

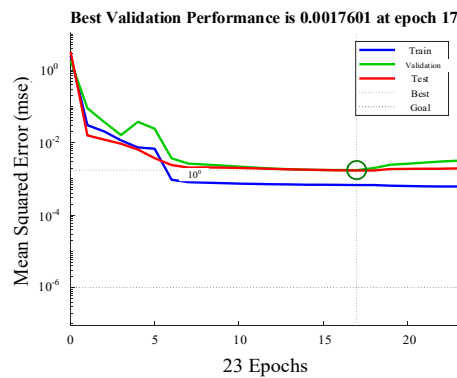


Figure 15. Error decline curve of neural network.

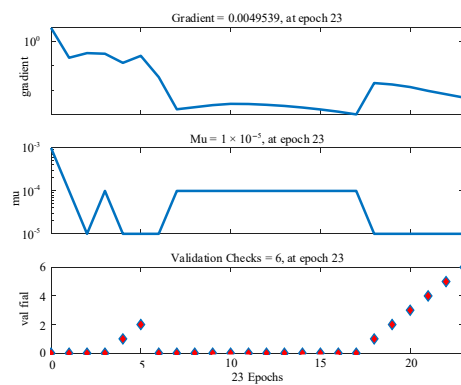


Figure 16. Neural network training process.

The average absolute percentage error between the predicted value and the expected value of the model was about 0.9%, with the relative error ranging between  $-2.63$  and

0.82%. The sum of square for overall prediction error stood at 0.17417, the average absolute error at 0.09057, the mean square error at 0.017417, the root mean square error at 0.13197, and the correlation coefficient R at 0.9983, respectively, indicating the high prediction accuracy and reliability of the experimental method. The prediction results of the model were compared through the error analysis, as shown in Figures 17 and 18:

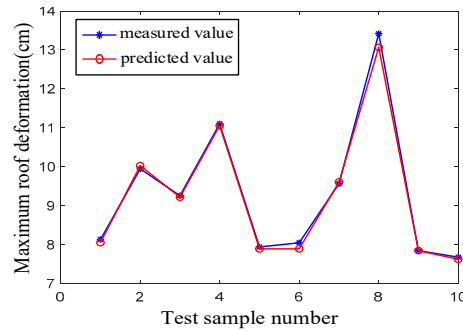


Figure 17. Comparison between predicted values and expected values of the BP test set.

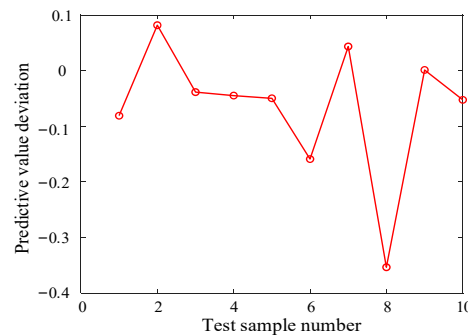


Figure 18. Errors of prediction results of maximum roof deformation.

The weight of each influencing factor was briefly calculated based on the data obtained, with the formula shown as follows:

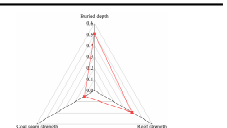
$$W_i = \frac{\left| \sum_{j=1}^q w_{ij}V_j \right|}{\sum_{i=1}^m \left| \sum_{j=1}^q w_{ij}V_j \right|} \tag{2}$$

where  $W_i$  stands for the weight of the influencing factor  $i$ ;  $W_{ij}$  denotes the connection weight between the  $i$ th node of the input layer and the  $j$ th node of the hidden layer;  $V_j$  is the connection weight between the  $j$ th node of the hidden layer and the node of the output layer;  $q$  refers to the number of hidden layer nodes, namely six herein;  $m$  represents the number of influencing factors, namely three herein.

The weight of each factor was calculated as shown in Table 5:

Table 5. Analysis of the weight of each influencing factor.

| Influencing Factor   | Weight Value | Sort |
|----------------------|--------------|------|
| Roadway buried depth | 0.5073       | 1    |
| Roof rock strength   | 0.3888       | 2    |
| Coal seam strength   | 0.1040       | 3    |



Based on the analysis of the weight, the roadway buried depth and the roof strength were determined as the major influencing factors for their significant impacts on the

maximum deformation of the roadway roof, while the coal seam strength was determined as the secondary influencing factor due to its minor impact.

The actual deformation of the roadway is predicted by the trained BP neural network model; the results are shown in Figure 19. It can be seen that the actual deformation is much smaller than the predicted value of the model because the support system played a role in the excavation.

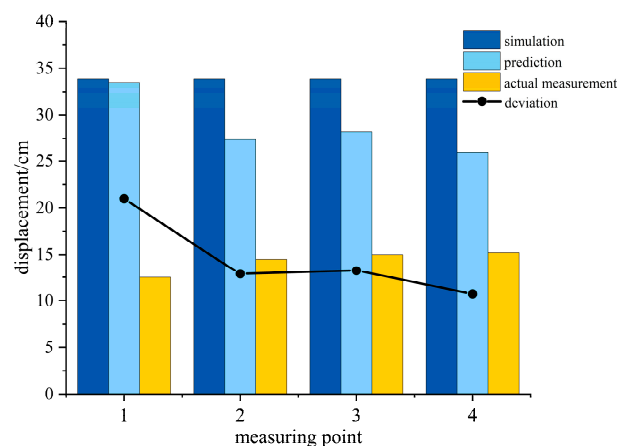


Figure 19. Prediction deviation curve.

## 5. Conclusions

This paper focuses on the influences of high dynamic load on the deformation and failure of roadway surrounding rocks, as well as on the prediction method for the deformation of roadway surrounding rocks. The major conclusions are listed as follows:

- (1) The buried depth of the roadway has a significant influence on stress distribution and deformation of surrounding rocks, and the deformation and stress concentration of the deep roadway are extremely severe. Under a large buried depth, the maximum deformation of the roof and the side even exceeded 1.5 m and 1.7 m, respectively, and the plastic zone mainly exists in the coal seam.
- (2) Compared with roof lithology, coal seam lithology exerts a smaller impact on roof deformation but a larger impact on side wall deformation. The peak stress at the center of the roof under C6 decreased by 43% from that under C1, while the vertical stress on the two sides decreased by 73%.
- (3) The increase of the side pressure coefficient in value affects the deformation of the roadway side significantly and the horizontal stress concentration area moves towards the roadway gradually. The impacts of different side pressures reduced the plastic failure range to a certain extent.
- (4) The BP neural network prediction theory was adopted to predict the deformation of roadway surrounding rocks. The average absolute percentage error between the predicted value and the measured value and the correlation coefficient  $R$  are measured as 0.90% and 0.9983, respectively, revealing favorable accuracy and reliability of the method. The relationship among the weight of each factor affecting roadway roof deformation is listed as follows: roadway buried depth > roof lithology > coal seam lithology.

**Author Contributions:** Data curation, A.L. and P.W.; formal analysis, A.L.; funding acquisition, J.K. (Jianguang Kan); investigation, A.L., G.C., X.W., and J.K. (Jiangrong Kong); methodology, A.L.; project administration, J.K. (Jianguang Kan); software, A.L. and Z.H.; writing—original draft, A.L.; Writing—review and editing, J.K. (Jianguang Kan) and P.W. All authors have read and agreed to the published version of the manuscript.

**Funding:** The paper was financially supported by the National Natural Science Foundation of China (52074263 and 52034007).

**Institutional Review Board Statement:** Not applicable.

**Informed Consent Statement:** Not applicable.

**Data Availability Statement:** Data for this study are available from the corresponding author upon reasonable request.

**Acknowledgments:** The authors thank anonymous colleagues for their kind efforts and valuable comments, which have improved this work.

**Conflicts of Interest:** The authors declare no conflict of interest.

## References

1. Dou, L.M.; He, J.; Cao, A.Y.; Gong, S.Y.; Cai, W. Rock burst prevention methods based on theory of dynamic and static combined load induced in coal mine. *J. China Coal Soc.* **2015**, *40*, 1469–1476. [\[CrossRef\]](#)
2. Liu, D.Q.; He, M.C.; Wang, C.C.; Wang, J.; Yang, J.; Wang, Y. Experimental study on rock burst induced by dynamic load. *J. China Coal Soc.* **2016**, *41*, 1099–1105. [\[CrossRef\]](#)
3. Wang, X.B.; Liu, T.X.; Tian, F.; Qian, S.S. Numerical simulation of tunnel roof cracking mechanism under periodic impact loads. *Meitan Xuebao* **2021**, *46*, 3106–3115. [\[CrossRef\]](#)
4. Wu, Y.Z.; Fu, Y.K.; He, J.; Chen, J.Y.; Chu, X.W.; Meng, X.Z. Principle and technology of “pressure relief-support-protection” collaborative prevention and control in deep rock burst roadway. *J. China Mine Soc.* **2021**, *46*, 132–144. [\[CrossRef\]](#)
5. Tang, J.P.; Zhang, X.; Pan, Y.S.; Hao, N. Experimental study on outburst and impact evolution characteristics of coal and gas in deep roadways. *Rock Mech. Rock Eng.* **2022**, *41*, 1081–1092. [\[CrossRef\]](#)
6. Wang, P.; Zhang, N.; Kan, J.G.; Xie, Z.Z.; Wei, Q.; Yao, W.H. Fiber Bragg Grating Monitoring of Full-bolt Axial Force of the Bolt in the Deep Strong Mining Roadway. *Sensors* **2020**, *20*, 4242. [\[CrossRef\]](#)
7. Wen, Z.J.; Jing, S.L.; Song, Z.Q.; Jiang, Y.J.; Tang, J.Q.; Zhao, R.L.; Xiao, Q.H.; Zhang, T.J.; Wang, H.T.; Zhao, H.B.; et al. Study on coal face spatial structure model and control related dynamic disasters. *Int. J. Coal Sci. Technol.* **2019**, *47*, 52–61. [\[CrossRef\]](#)
8. Xie, S.R.; Wang, E.; Chen, D.D.; Jiang, Z.S.; Li, H.; Liu, R.P. Collaborative control technology of external anchor-internal unloading of surrounding rock in deep large-section coal roadway under strong mining influence. *China Coal Soc.* **2022**, *47*, 1946–1957. [\[CrossRef\]](#)
9. Naji, A.M.; Rehman, H.; Emad, M.Z.; Ahmed, S.; Kim, J.J.; Yoo, H. Static and Dynamic Influence of the Shear Zone on Rockburst Occurrence in the Headrace Tunnel of the Neelum Jhelum Hydropower Project, Pakistan. *Energies* **2019**, *12*, 2124. [\[CrossRef\]](#)
10. Fan, C.J.; Li, S.; Elsworth, D.; Han, J.; Yang, Z.H. Experimental investigation on dynamic strength and energy dissipation characteristics of gas outburst prone coal. *Energy Sci. Eng.* **2022**, *8*, 1015–1028. [\[CrossRef\]](#)
11. Jia, C.; Li, S.; Fan, C.J.; Tang, J.B. Numerical Simulation of Mechanical Characteristics of Roadway Surrounding Rock under Dynamic and Static Loading. *Shock Vib.* **2021**, *2021*, 1869583. [\[CrossRef\]](#)
12. Xie, Y.Y.; Meng, Z.S.; Zeng, Q.L.; Yang, C.X.; Gao, K.D. Analysis of distribution characteristics of study on floor specific pressure of hydraulic support for deep mining based on impact loading. *J. China Coal Soc.* **2020**, *45*, 982–989. [\[CrossRef\]](#)
13. Li, X.F. Research on rock fracturing and fragmentation subject to intensive impact loading. *Rock Mech. Rock Eng.* **2021**, *40*, 432. [\[CrossRef\]](#)
14. Wang, P.; Zhang, N.; Kan, J.G.; Wang, B.; Xu, X.L. Stabilization of Rock Roadway under Obliquely Straddle Working Face. *Energies* **2021**, *14*, 5759. [\[CrossRef\]](#)
15. Mu, C.M.; Gong, N.P. Damage mechanism of coal under impact loads. *Meitan Xuebao* **2017**, *42*, 2011–2018. [\[CrossRef\]](#)
16. Han, Y.D. Research on Surrounding Rock Control Technology of Strong Dynamic Pressure Roadway in Isolated Island Working Face. Master’s Thesis, China University of Mining and Technology, Xuzhou, China, 2021. [\[CrossRef\]](#)
17. Meng, Q.B.; Han, L.J.; Chen, Y.L.; Fan, J.D.; Wen, S.Y.; Yu, L.Y.; Li, H. Influence of dynamic pressure on deep under ground soft rock roadway support and its application. *Int. J. Min. Sci. Technol.* **2016**, *26*, 903–912. [\[CrossRef\]](#)
18. Zhu, Z.D.; Sun, L.Z.; Wang, M.Y. Damping ratio experiment and mesomechanical analysis of deformation failure mechanism on rock under different frequency cyclic loadings. *Rock Soil Mech.* **2010**, *31*, 8–12. [\[CrossRef\]](#)
19. Wu, P.F.; Yang, T.J.; Jia, W.C. Reliability Analysis and Prediction on Tunnel Roof under Blasting Disturbance. *KSCE J. Civ. Eng.* **2019**, *23*, 4036–4046. [\[CrossRef\]](#)
20. Liu, X.S.; Fan, D.Y.; Tan, Y.L.; Wang, X.; Alexey, A. Failure and instability mechanism of anchored surrounding rock for deep chamber group with super-large section under dynamic disturbances. *Rock Soil Mech.* **2021**, *42*, 3407–3418. [\[CrossRef\]](#)
21. Naji, A.M.; Rehman, H.; Emad, M.Z.; Ahmed, S.; Kim, J.J.; Yoo, H. Rockburst evaluation in complex geological environment in deep hydropower tunnels. In *Tunnels and Underground Cities: Engineering and Innovation meet Archaeology, Architecture and Art*; CRC Press: Boca Raton, FL, USA, 2019; pp. 1002–1009. [\[CrossRef\]](#)
22. Wang, S.C. Simulation Experiment of Surrounding Rock Deformation and Failure Induced by Mining Dynamic Load. Master’s Thesis, China University of Mining and Technology, Xuzhou, China, 2017.
23. Li, C.; Zhang, W.L.; Wang, N.; Hao, C. Roof stability control based on plastic zone evolution during mining. *J. Min. Saf. Eng.* **2019**, *36*, 753–761. [\[CrossRef\]](#)
24. Xiao, Z.M.; Liu, J.; Wang, H.; Sun, L.; Zhou, H. Study on Mechanism and Control of Rock Burst Instability of Roadway Floor Induced by Dynamic Load Disturbance. *Chin. J. Undergr. Space Eng.* **2019**, *15*, 1573–1581.

25. Feng, J.C.; Yin, S.F.; Cheng, Z.H.; Shi, J.J.; Shi, H.Y.; Xu, H.T.; Guo, S.Y. Deformation and Failure Mechanism of Surrounding Rock in Mining-Influenced Roadway and the Control Technology. *Shock. Vib.* **2021**, *2021*, 5588314. [[CrossRef](#)]
26. Wang, J.C.; Wang, Z.H. Impact Effect of Dynamic Load Induced by Roof in High-Intensity Mining Face. *Rock Mech. Rock Eng.* **2015**, *34*, 3987–3997. [[CrossRef](#)]
27. Wang, P.; Zhang, N.; Kan, J.G.; Xu, X.L.; Cui, G.Z. Instability Mode and Control Technology of Surrounding Rock in Composite Roof Coal Roadway under Multiple Dynamic Pressure Disturbances. *Geofluids* **2022**. [[CrossRef](#)]
28. Chen, G.X.; Dou, L.M.; Gao, M.S.; Mu, Z.L. Numerical Simulation of Dynamic Vibration Affecting Rock Burst in Mining Gateway Caused by Tremor. *J. Min. Saf. Eng.* **2009**, *26*, 153–157. [[CrossRef](#)]
29. Zhang, X.T.; Dou, L.M. Numerical Simulation of the Influence of Hardness and Thickness of Coal Seam on Rock Burst. *J. Min. Saf. Eng.* **2006**, *3*, 277–280. [[CrossRef](#)]
30. Zhang, X.C.; Lu, A.H.; Wang, J.Q. Numerical Simulation of Layer-Crack Structure of Surrounding Rock and Rockburst in Roadway under Dynamic Disturbance. *Rock Mech. Rock Eng.* **2006**, *25*, 3110–3114. [[CrossRef](#)]
31. Kan, J.G.; Li, G.C.; Zhang, N.; Wang, P.; Han, C.L.; Wang, S. Changing characteristics of sandstone pore size under cyclic loading. *Geofluids* **2021**, *2021*, 6664925. [[CrossRef](#)]
32. He, F.L.; Zhang, G.C. Deformation and failure mechanism and control technology of large section coal roadway subjected to severe mining dynamic load. *J. Min. Saf. Eng.* **2016**, *33*, 423–430. [[CrossRef](#)]
33. Zhao, H.B.; Wang, Z.W.; Zhang, H.; Li, W. Effects of dynamic loads on development of internal microstructure and distribution of new surface fractures of coal. *Rock Mech. Rock Eng.* **2016**, *35*, 971–979. [[CrossRef](#)]
34. Li, Y.Y.; Zhang, S.C.; Wen, Z.J.; Zhao, R.L.; Cao, Z.G.; Lun, Q.Z.; Bai, J.Z. Energy conversion and fragment distribution characteristics of coal sample under uniaxial cyclic loading. *J. China Coal Soc.* **2019**, *44*, 1411–1420. [[CrossRef](#)]
35. Wang, Z.Y.; Dou, L.M.; Wang, G.F.; Li, J. Research on Dynamic Response of Anchoring Roadway Surrounding Rock Structure. *J. China Univ. Min. Technol.* **2016**, *45*, 1132–1140. [[CrossRef](#)]
36. Xia, Z.X. Study on the effect of explosive stress wave in coal roadway and its wartime application. Ph.D. Thesis, China University of Mining and Technology, Xuzhou, China, 2004.
37. Wang, T. Research and Application of Deformation Mechanism of Surrounding Rock with Bedding Surface in High Street Road. Ph.D. Thesis, China University of Mining and Technology, Xuzhou, China, 2021. [[CrossRef](#)]
38. Li, S.J.; Liu, Y.X.; Wang, D.G.; Li, H.; Wu, F.J. Inversion Algorithm of Permeability Coefficients of Rockmass and Its Application Based on Artificial Neural Network. *Rock Mech. Rock Eng.* **2002**, *21*, 479–483. [[CrossRef](#)]

**Disclaimer/Publisher’s Note:** The statements, opinions and data contained in all publications are solely those of the individual author(s) and contributor(s) and not of MDPI and/or the editor(s). MDPI and/or the editor(s) disclaim responsibility for any injury to people or property resulting from any ideas, methods, instructions or products referred to in the content.